Characterisation of Varying Iron Ores and Their Thermal Decomposition Kinetics Under HIsarna Ironmaking Conditions

Leerhoff, P.; Brouwer, J.C.; Mohseni Armaki, A.; Zeilstra, Christiaan; Meijer, Koen; van der Stel, Jan; Abrahami, S.T.; Dogan, N.D.; Yang, Y.

DOI
10.3390/met14111271

Publication date
2024

Document Version
Final published version

Published in
Metals

metals

MDPI

Article

Characterisation of Varying Iron Ores and Their Thermal Decomposition Kinetics Under HIsarna Ironmaking Conditions

Philipp Leerhoff [1,*], Johannes C. Brouwer [1], Amir Mohseni Armaki [1], Christiaan Zeilstra [2], Koen Meijer [2], Jan van der Stel [2], Shoshan T. Abrahami [1], Neslihan Dogan [1] and Yongxiang Yang [1]

[1] Department of Materials Science and Engineering, Delft University of Technology, 2628 CD Delft, The Netherlands
[2] Tata Steel Netherlands, 1970 CA IJmuiden, The Netherlands
* Correspondence: p.leerhoff@tudelft.nl

Abstract: In the pre-reduction cyclone of the HIsarna process, both thermal decomposition and gas reduction of the injected iron ores occur simultaneously at gas temperatures of 1723–1773 K. In this study, the kinetics of the thermal decomposition of three iron ores (namely OreA, OreB and OreC) for HIsarna ironmaking were analysed as an isolated process with a symmetrical thermogravimetric analyser (TGA) under an inert atmosphere. Using various methods, the chemical and mineralogical composition, particle size distribution, morphology and phase distribution of the ores were analysed. The ores differ in their mineralogy and morphology, where OreA only contains hematite as iron-bearing phase and OreB and OreC include goethite and hematite. To obtain the kinetic parameters in non-isothermal conditions, the Coats–Redfern Integral Method was applied for heating rates of 1, 2 and 5 K/min and a maximum temperature of 1773 K. The TGA results indicate that goethite and hematite decomposition occur as a two-stage process in an inert atmosphere of Ar. The proposed reaction mechanism for the first stage of goethite decomposition is chemical reaction with an activation energy ranging from 46.55 to 60.38 kJ/mol for OreB and from 69.90 to 134.47 kJ/mol for OreC. The proposed reaction mechanism for the second stage of goethite decomposition is diffusion, showing an activation energy ranging between 24.43 and 44.76 kJ/mol for OreB and between 3.32 and 23.29 kJ/mol for OreC. In terms of hematite decomposition, only the first stage was analysed. The proposed reaction mechanism is chemical reaction control. OreA shows an activation energy of 545.47 to 670.50 kJ/mol, OreB one of 587.68 to 831.54 kJ/mol and OreC one of 424.31 to 592.32 kJ/mol.

Keywords: HIsarna ironmaking; iron ore; thermal decomposition; kinetics; extractive metallurgy

Citation: Leerhoff, P.; Brouwer, J.C.; Armaki, A.M.; Zeilstra, C.; Meijer, K.; van der Stel, J.; Abrahami, S.T.; Dogan, N.; Yang, Y. Characterisation of Varying Iron Ores and Their Thermal Decomposition Kinetics Under HIsarna Ironmaking Conditions. *Metals* **2024**, *14*, 1271. https://doi.org/10.3390/met14111271

Academic Editor: Antoni Roca

Received: 26 September 2024
Revised: 31 October 2024
Accepted: 5 November 2024
Published: 8 November 2024

1. Introduction

The iron- and steelmaking industry alone is responsible for around 7–9% of anthropogenic-generated CO_2 emissions [1]. The main reason for this is the blast furnace (BF), which is the dominant operating technology for ironmaking, contributing up to 71% of the global CO_2 emissions for steel production [2]. Comparing the currently commercially available established steelmaking routes, BF-BOF, Scrap-EAF, and DRI-EAF, the blast furnace route exhibits the highest amounts of CO_2 emissions per tonne of crude steel [2]. Our society is strongly dependent on steel production and considering the increasing production trend over last few decades, steel production is expected to grow further [3], and it is of utmost importance to reduce the CO_2 emissions arising from the steel industry.

Iron ores can generally be categorised into high-grade (>65% Fe), medium-grade (62–65% Fe) and low-grade (<62% Fe) ores. The most commercially used iron ores are hematite (69.94% Fe) and magnetite (72.36% Fe), exhibiting the highest amounts of iron content in available ores. Next to hematite and magnetite, multiple other iron ores are present [4]. One of them is goethite, which is abundantly available in India [5]. Goethite ($FeO^*(OH)^*nH_2O$), a medium-grade ore, contains chemically bound water [4]. Alongside

the environmental problems arising from the blast furnace route, demand issues in the primary production of steel can become critical. Large amounts of goethite are important to tackle future demand problems in ironmaking industry, but its use leads to technical challenges due to its lower iron content.

In the framework of the ULCOS project, HIsarna (Figure 1) was developed by Tata Steel Netherlands as an alternative ironmaking process with the objective to substitute the blast furnace [6]. HIsarna operates using a counter-current principle, where the injected iron ore is in contact with the hot process gas in a temperature range of 1723–1773 K, thereby combining the two process steps of cyclone converter and smelting reduction in a single operating furnace [7]. In the upper section, the solid particles are heated up, melted and pre-reduced with reducing gas mixtures of CO-CO_2-H_2-H_2O, arising from the reactions in the lower section of the furnace [7,8]. In the lower section of the furnace, the final reduction of the pre-reduced molten ores with coal to metallic iron takes place. Due to this reaction, the reducing gas mixture needed in the top section is produced [7]. The degree of pre-reduction that occurs in the top section is around 10–20%. The use of HIsarna, instead of the blast furnace, reduces the three blast furnace process steps, coking, agglomeration and ironmaking, to only one process step, the ironmaking itself. This leads to a lower energy consumption and less CO_2 emissions [7]. In combination with carbon capture and storage (CCS) technology, HIsarna is expected to reduce CO_2 emissions by up to 80% compared to traditional blast furnace ironmaking [8]. HIsarna has the further advantage of using low-grade, untreated (industrial) ores, with a high amount of gangue material, which are lower in iron content and other residues arising from iron-bearing processes within and outside the steelmaking industry. Further, hydrogen enrichment and the use of renewable carbon sources to improve HIsarna ironmaking technologies are under investigation.

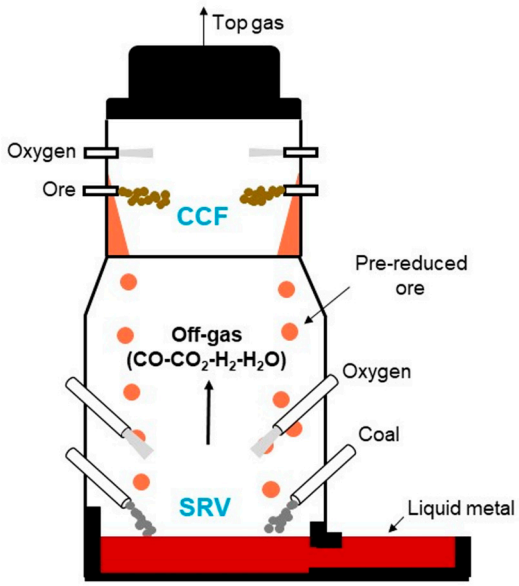

Figure 1. Schematic of HIsarna process (Adapted from [7]).

In the top section of a HIsarna furnace, two main reaction mechanisms prevail: thermal decomposition and gas–solid reduction by a gas mixture of CO and H_2. During the injection, the fine ores are rapidly heated up, thermally decomposed, pre-reduced by the gas atmosphere and partly melted. Most particles experience short residence times in the top section of the HIsarna furnace, but some particles can hit the walls and become deposited as a molten film. Considering thermodynamics, the reduction of the ores by thermal decomposition and gas reduction has the same effect. Both reactions describe the removal of oxygen from the ore leading to a lower oxygen content. Regarding kinetics,

however, both the residence time of the particle in the top section and the mechanisms that occur influence the reaction rates and rate-limiting steps. Qu et al. [9] investigated the thermal decomposition behaviour of hematite ores with low gangue materials and Chen et al. [10] focused on the thermal decomposition behaviour of hematite ores with higher gangue contents. The current study aims to extend this research to the investigation of hematite ores with high contents of gangue materials as well as goethite-based iron ores and to analyse the influence of ore mineralogy on the decomposition kinetics.

2. Material Analysis

Varying types of commercial iron-bearing ores were provided by Tata Steel Netherlands, which we called OreA, OreB and OreC. The ores were classified into two different particle size fractions (<63 µm, (63–125) µm) by wet sieving. The particle size is defined as the particle diameter. The size ranges were verified via light scattering technology with the Microtrac Bluewave. Each sample was automatically measured in triplicate. The resulting mean diameter of the volume distribution (MV), number distribution (MN) and area distribution (MA) are presented in Table 1 and the overall particle size distribution in Figure 2. It is important to mention that the three values of MV, MN and MA are used to generate a broad overview on the averaged particle sizes from different perspectives. MV is strongly influenced by coarser particles and therefore usually shows larger average particle sizes. MA is a particle surface measurement and is less affected by coarse particles, leading to smaller average particle sizes. MN is related to the population of the particles and is more sensitive towards small particles, therefore showing the smallest average particle size. Figure 2 portrays the passing percentage in relation to the particle size. A larger passing at low particle sizes, therefore indicates an overall smaller particle size distribution. The <63 µm fractions of OreA, OreB and OreC show almost no particles larger than the defined fraction. The fraction of (63–125) µm OreC shows the largest passing in the defined ranges, followed by OreB and OreA.

Table 1. Mean particle size values for varying iron ores.

	OreA		**OreB**		**OreC**	
Fraction [µm]	<63	63–125	<63	63–125	<63	63–125
MV [µm]	50.74	103.6	44.22	100.2	22.79	115.9
MN [µm]	19.55	51.96	3.66	66.29	1.106	89.55
MA [µm]	39.41	84.86	25.52	87.58	6.80	105.5

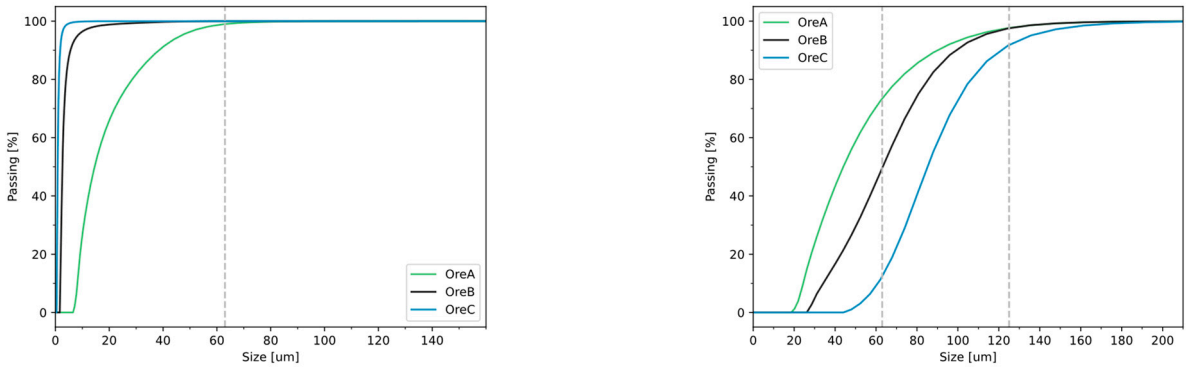

Figure 2. Particle size distribution of OreA, OreB and OreC for size fractions of (**a**) <63 µm and (**b**) (63–125) µm.

2.1. Composition Analysis

X-Ray diffraction (XRD) with a Bruker D8 Advance diffractometer Bragg-Brentano geometry and Lynxeye position sensitive detector (Bruker, Germany) was used to evaluate the mineralogy of the samples and to determine the main differences in composition of the different iron ores. In general, the XRD signal is complex, containing a lot of smaller peaks due to the high amount of gangue materials in the ores (Figure S1, Supplementary Materials). For OreA, hematite (Fe_2O_3), quartz (SiO_2) and dolomite ($CaMg(CO_3)_2$ were detected as the main phases. Additionally, for the fraction < 63 µm a few small magnetite (Fe_3O_4) peaks occurred, which were not measured in the other samples. OreB and OreC contained a goethite phase as an iron-bearing mineral in addition to hematite. The mineralogical composition of OreB was goethite (FeOOH), hematite, quartz and kaolinite ($Al_2Si_2O_5(OH)_4$). For OreC only hematite, goethite and quartz were detected as mineral phases.

In order to obtain deeper insights in the elemental composition of the ores, the chemical compositions of the ore fractions were determined by X-Ray fluorescence (XRF) (Panalytical AXIOS XRF, Netherlands) and loss of ignition (LOI) analysis (dissolution in nitric acid and TGA (LECO, Germany)). The results are listed in Table 2, after normalisation and conversion to the expected oxide phases. The total-C in the system was calculated based on the assumption that all measured carbon is present as CO_2 in the sample. The content of gangue and iron-bearing phases varies not only between the different ores, but also between the different size fractions. For all ores, the main gangue components were SiO_2 and Al_2O_3. OreB shows the highest amounts of Al_2O_3, underlined by the detected kaolinite phase in the XRD measurements. All ores show similar contents of SiO_2, varying in particle size fraction. In contrast to OreB and OreC, the measurements for OreA show higher amounts of CaO and MgO, from the detected dolomite phase. Further, OreB and OreC show lower amounts of carbon compared to OreA, due to the association of carbon to the dolomite phase in OreA. The crystal water in OreB and OreC indicates a goethite phase, with larger amounts present in OreC.

Table 2. Chemical composition of varying iron ores based on XRF and LOI.

		OreA		**OreB**		**OreC**	
	Fraction [µm]	**<63**	**63–125**	**<63**	**63–125**	**<63**	**63–125**
Compound [wt.%]	Fe_2O_3	85.93	91.50	88.07	85.07	81.21	82.92
	total-Fe	60.10	64.00	61.60	59.50	56.80	58.00
	SiO_2	5.18	2.96	4.96	5.83	6.84	5.30
	Al_2O_3	2.24	1.44	3.81	4.78	3.52	3.00
	MgO	0.71	0.41	0.04	0.04	0.14	0.11
	CaO	1.99	1.23	0.05	0.05	0.11	0.07
	TiO_2	1.04	0.92	0.33	0.35	0.18	0.16
	MnO	1.20	0.60	0.03	0.03	1.07	1.24
	total-C	0.41	0.23	0.06	0.07	0.18	0.14
	H_2O(crystal)	-	-	2.19	3.26	6.05	6.39
	Rest	0.37	0.21	0.25	0.31	0.26	0.26

2.2. Morphological Analysis

To observe the morphology of the different ores, SEM images were taken by a Jeol JSM-IT100 (Jeol, The Netherlands). Representative images of the chosen fractions of the ores are displayed in Figure 3. Significant differences in morphology are visible between the goethite and hematite ores. The morphology of OreA appears to be angular in shape with almost no spherical particles. The structure is close-grained and does not seem to be porous. Bright particles assumed to be further gangue components, are visible either as individual particles or as inclusions on the hematite particles. OreB appears to be less angular and more spherical in structure. The presence of crystal water could be a reason for the apparent porosity of the particles. For OreC, the particles of the larger size fraction (Figure 3f) again appear to be more close-grained, despite the larger amounts of crystal

water. Again, the particles shape appears to be more spherical compared to OreA. However, for the <63 µm size fraction (Figure 3c), the particles seem to agglomerate and many fine ore particles are observable as clusters. This is also reflected in the low average particle size values of MV, MN and MA of this fraction. For OreB and OreC no bright particles are visible either on the particle surface or as individual particles.

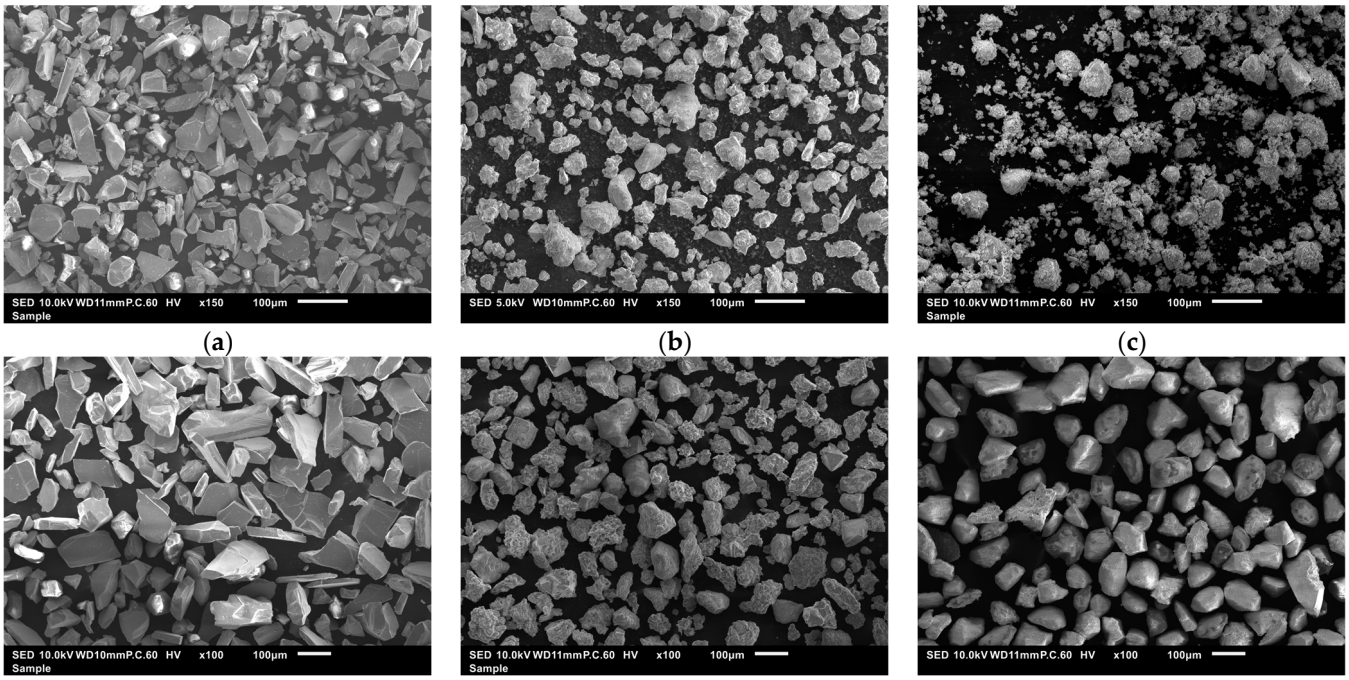

Figure 3. SEM images for (**a**) OreA fraction < 63 µm (150×); (**b**) OreB fraction < 63 µm (150×); and (**c**) OreC fraction < 63 µm (150×); (**d**) OreA fraction (63–125) µm (100×); (**e**) OreB fraction (63–125) µm (100×); and (**f**) OreC fraction (63–125) µm (100×).

2.3. Phase Distribution

To further investigate the distribution of impurities (gangue) in the samples, the particles of the small fractions (<63 µm) were mounted in a resin, followed by sanding and polishing to create a cross-section of the particles. The cross-sections were again analysed under the SEM, together with EDS mapping to gain insight into the elemental distribution of the particles (Figure 4). Displayed here are only the main elements of the ore, Fe, Al and Si. The mapping of OreA supports the findings from the morphological study, indicating that the distribution of impurities is seen as single, brighter particles, as well as inclusions on the hematite particles. The elemental distribution of OreC indicates a similar distribution compared to OreA. Aluminium and silicon are distributed as distinct particles across the sample, with high intensities of these elements. For OreB, a different elemental distribution is observable. For silicon, a few distinct small particles are visible. Apart from that, the aluminium and silicon compounds seem to be coexisting with the iron ore particles. However, the distribution of iron shows that several iron ore particles are present without the additional presence of aluminium or silicon.

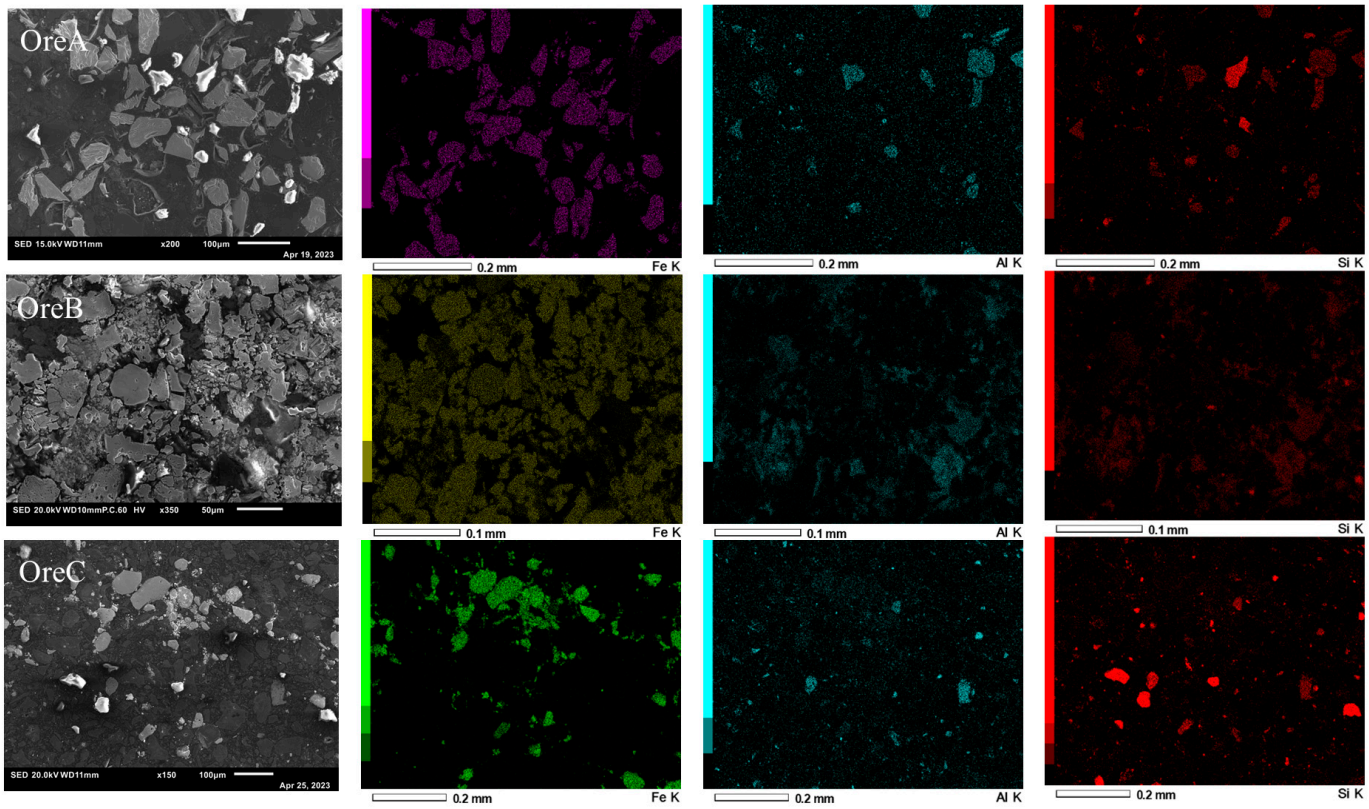

Figure 4. Elemental distribution of ore fractions < 63 µm in mounted resin (purple/yellow/green: Fe, blue: Al, red: Si).

It is not possible to distinguish between hematite and goethite using SEM-EDS due to the elemental characteristics of hydrogen. To gain more insights into the distribution of the goethite phase in OreB and OreC, surface-enhanced Raman spectroscopy (alpha300 R-Raman imaging microscope (WITec, Ulm, Germany)) was carried out for both size fractions of OreB and OreC (Figure 5). Data from the literature for pure hematite and goethite [11] were used to identify pure hematite and goethite particles in the samples. Based on the Raman shift in these particles, the reference spectrum presented in Figure 5a was created to map the phase distribution. Next, different representative spots in the samples were measured and compared to the reference spectra. If the shift in the peaks is similar to the reference spectra, it is assumed to be the same phase. Apart from the pure goethite and hematite, a mixed phase was measured, shown in the example spectrum in Figure 5b.

Considering the distribution of goethite and hematite in the large size fraction (63–125 µm), four different particle structures were identified for both OreB and OreC (Figure 5d,f). OreC consists of almost pure hematite and goethite particles, hematite particles with smaller amounts of goethite and goethite particles with distinctive hematite inclusions and a mixed phase. OreB also contains almost pure hematite and goethite particles. However, goethite particles with hematite inclusions and the mixed phase appear to be present in larger quantities. For the smaller size fraction (<63 µm), no individual particles were analysed, but a selected area was scanned for the mapping. It must be noted that the dark area in the scan relates to the resin the particles were embedded in. OreC in Figure 5c shows a distinctive separation of the goethite and hematite phase and small spots of the mixed phase. OreB in Figure 5e also shows a segregation of the hematite and goethite phases. However, the mapping of OreB further indicates the co-existence of goethite and hematite in some areas.

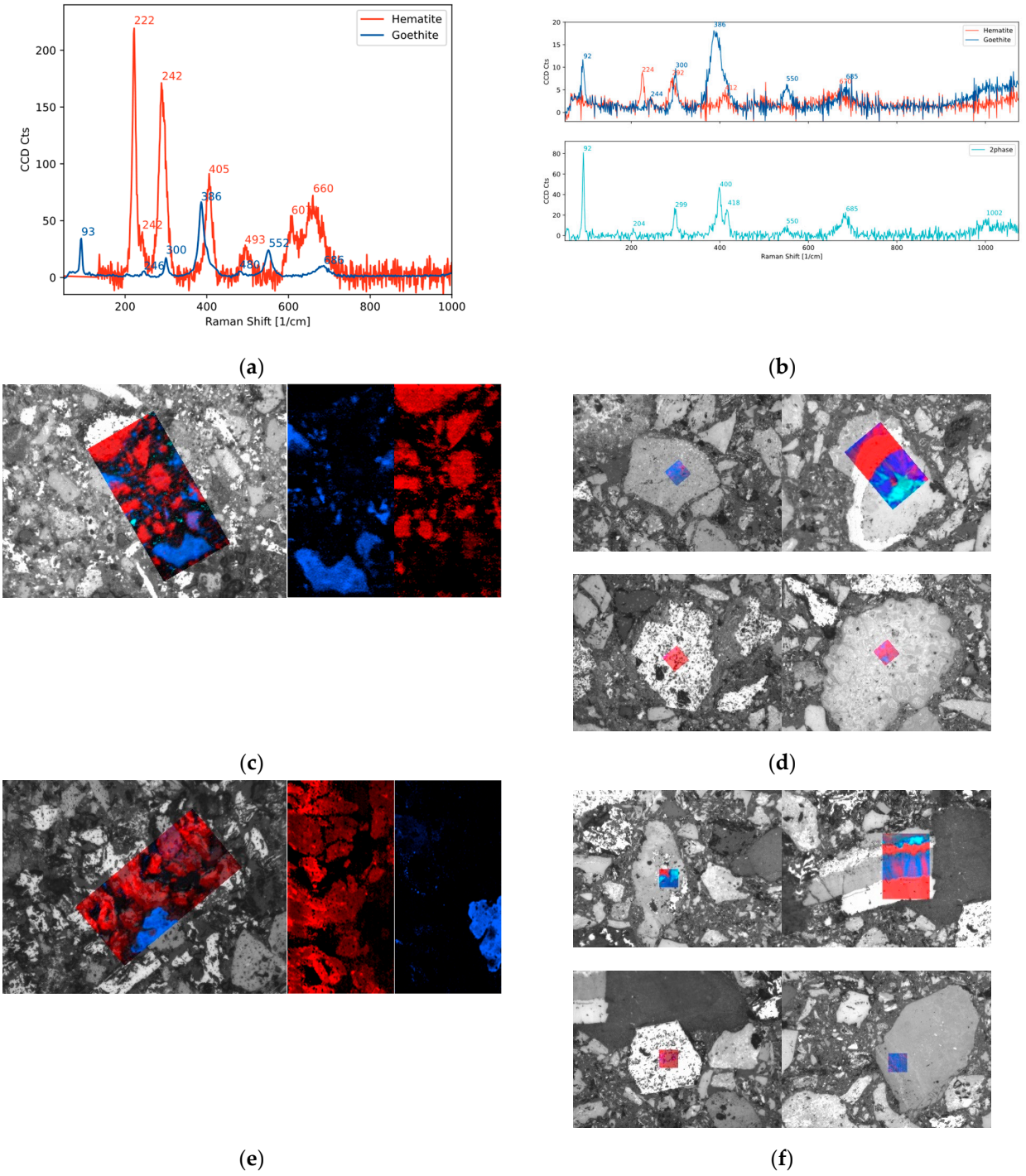

Figure 5. Raman spectroscopy for (**a**) the reference spectra; (**b**) the spectra of OreC < 63 µm; (**c**) mapping for OreC < 63 µm (left for complete mapping; right for separated mapping); (**d**) OreC (63–125) µm; (**e**) OreB < 63 µm (left for complete mapping; right for separated mapping); and (**f**) OreB (63–125) µm (red: hematite, dark blue: goethite, light blue: mixed phase).

3. Methods

3.1. TGA Experiments

To obtain insights into the non-isothermal decomposition behaviour and kinetics of the goethite and hematite ores, experiments were carried out in a symmetrical thermogravimetric analyser (TGA, Setaram TAG 16/18, Caluire, France). Around 300 mg of ore sample was placed into Alsint crucibles with an inner diameter of 10 mm and a wall thickness of

2 mm. The total height of the crucible is 20 mm. The operating parameters are presented in Table 3. In order to evaluate the thermal decomposition of the ores, the experiments were carried out in an argon atmosphere with a flow rate of 100 mL/min. The ore particles with a size fraction < 63 µm were gradually heated at three heating rates (1, 2 and 5 K/min) until a temperature of 1773 K was reached. Experiments for the particle size fraction of (63–125) µm were only carried out with a heating rate of 2 K/min to compare the results to the smaller particle size fraction at the same heating rate. After 1773 K was reached, a holding time of two hours was applied to achieve the limit of thermal decomposition. After that, the system was cooled to room temperature with a controlled cooling rate of 5 K/min. The mass loss over an increasing temperature at a constant heating rate was measured as the basic data for performing the decomposition and kinetic analysis.

Table 3. Experimental conditions in TGA, Setaram TAG 16/18.

Experimental Condition	Operating Parameter
Sample	Hematite fine ore, Goethite fine ore
Holding time (h)	2
Heating rate (K/min)	1, 2, 5
Particle size (µm)	<63, 63–125
Temperature (K)	298–1773
Atmosphere	Ar

3.2. Assessment of Reaction Kinetics of Thermal Decomposition

The kinetic parameters, activation energy (Ea) and pre-exponential factor A of hematite and goethite decomposition under non-isothermal conditions with a constant heating rate were determined using the Coats–Redfern Integral Method [12]. Through model fitting, the most applicable model describing the thermal decomposition of hematite and goethite was estimated. Commonly used models for gas–solid reactions are listed in Table 4. The essential characteristic parameter for all the kinetic models is the conversion factor α (Equation (1)).

$$\alpha = \frac{m_0 - m_t}{m_0 - m_a} \quad (1)$$

where m_0 is the mass of the initial sample (mg), m_t is the mass of the sample at time t (mg) and m_a is the mass of the sample after complete conversion or thermal decomposition (mg). In the following analysis, the final conversion state was considered to be the decomposition from either Fe_2O_3 to Fe_3O_4 or from FeOOH to Fe_2O_3. Hence, a conversion factor of 0 equals the initial state of hematite or goethite and a conversion factor of 1 equals the complete decomposition to magnetite or hematite. The general expression of the reaction rate of the thermal decomposition process is presented in (Equation (2)). Applying the Arrhenius equation, the expression for the reaction rate constant can be determined through (Equation (3)). Considering a constant heating rate, the reaction rate equation can be written as (Equation (4)).

$$\frac{d\alpha}{dt} = kf(\alpha) \quad (2)$$

$$k = A\exp\left(-\frac{E_a}{RT}\right) \quad (3)$$

$$\frac{d\alpha}{dT} = \frac{A}{\beta}\exp\left(-\frac{E_a}{RT}\right)f(\alpha) \quad (4)$$

where k is the reaction rate constant (s^{-1}), f(α) is a function of the conversion factor α, A is the exponential factor (s^{-1}), E_a is the activation energy (J/mol), β is the heating rate (K/s), T is the temperature (K) and R is the gas constant (8.314 J/(mol·K). The kinetic parameters

of hematite and goethite decomposition were determined by the Coats–Redfern Integral Method (Equation (5)).

$$\ln\left[\frac{g(\alpha)}{T^2}\right] = \ln\left[\frac{AR}{\beta E_a}\left(1-\frac{2RT}{E_a}\right)\right] - \frac{E_a}{RT} \quad (5)$$

where $g(\alpha)$ is the integrated form of the function $f(\alpha)$. The activation energy (E_a) and pre-exponential factor (A) can be determined from the slope and intercept of the plot $\ln\left[\frac{g(\alpha)}{T^2}\right]$ vs.$\frac{1}{T}$. Assuming that the value of the activation energy is significantly larger then (2RT), the term $\left(1-\frac{2RT}{E_a}\right)$ in (Equation (5)) is assumed to equal to 1. Following, the slope of the plot equals $-\frac{E_a}{R}$ and the intercept equals $\ln\left[\frac{AR}{\beta E_a}\right]$. For the calculation of the activation energy, the intercept, reaction rate constant and the resulting reaction rate of the model with the best linear fit (R^2 close to 1) was used.

Table 4. Reaction models for gas–solid reaction processes (Adapted from [10,13]).

Reaction Model			f(α)	g(α)
Nucleation	Power law	P1	$4\alpha^{3/4}$	$\alpha^{1/4}$
		P2	$3\alpha^{2/3}$	$\alpha^{1/3}$
		P3	$2\alpha^{1/2}$	$\alpha^{1/2}$
		P4	$2/3\alpha^{-1/2}$	$\alpha^{3/2}$
	Avrami–Erofeev	A2	$2(1-\alpha)[-\ln(1-\alpha)]^{1/2}$	$[-\ln(1-\alpha)]^{1/2}$
		A3	$3(1-\alpha)[-\ln(1-\alpha)]^{2/3}$	$[-\ln(1-\alpha)]^{1/3}$
		A4	$4(1-\alpha)[-\ln(1-\alpha)]^{3/4}$	$[-\ln(1-\alpha)]^{1/4}$
Diffusion	n-Dimensional Diffusion	D1	$1/(2\alpha)$	α^2
		D2	$[-\ln(1-\alpha)]^{-1}$	$(1-\alpha)\ln(1-\alpha)+\alpha$
		D3	$3/2(1-\alpha)^{2/3}[1-(1-\alpha)^{1/3}]^{-1}$	$[1-(1-\alpha)^{1/3}]^2$
Geometrical Contraction	Contracting Area	R2	$2\times(1-\alpha)^{1/2}$	$1-(1-\alpha)^{1/2}$
	Contracting Volume	R3	$3\times(1-\alpha)^{2/3}$	$1-(1-\alpha)^{1/3}$
Reaction order	n-Order	F0	1	a
		F1	$1-\alpha$	$-\ln(1-\alpha)$
		F2	$(1-\alpha)^2$	$(1-\alpha)^{-1}-1$
		F3	$(1-\alpha)^3$	$[(1-\alpha)^{-2}-1]/2$

4. Results and Discussion

Even though most fine ores injected into the HIsarna furnace experience very short residence times (ms) in the pre-reduction cyclone of the system, particles can agglomerate in clusters or deposit on the walls of HIsarna furnace, leading to longer particle residence times. Gas reduction and thermal decomposition are expected to occur as co-existing phenomena. This paper studies the limits of thermal decomposition as an isolated mechanism of the presented ores. The Results section will first focus on the general thermal decomposition behaviour of the varying ores to identify the different decomposition stages and their temperature ranges. For this, the mass loss and QMS (quadrupole mass spectrometer) off-gas data will be presented. Based on the mass loss's dependency on temperature, a kinetic analysis is further carried out. First, the conversion factor will be determined as an underlying kinetic parameter for the defined temperature ranges and applied to the model fit. Based on the model fit, the activation energy for the varying iron ores will be compared.

4.1. Thermal Decomposition

Figure 6 shows different mass loss curves from the thermogravimetric measurement of the feed materials with particle size fractions of OreA, OreB and OreC with varying heating rates (Figure 6a) and a comparison to the larger particle size of (63–125) µm is shown in Figure 6b. Three mass loss stages are observed for OreA, while four stages are seen for OreB and OreC. The initiation of the individual mass loss curves shows slight dependencies

on the heating rate for all ores. The mass loss and therefore the decomposition starts earlier with lower heating rate. Larger dependencies are visible for the ores based on mineralogy. OreC shows the highest mass loss, while OreA shows the lowest mass loss under the same thermal conditions.

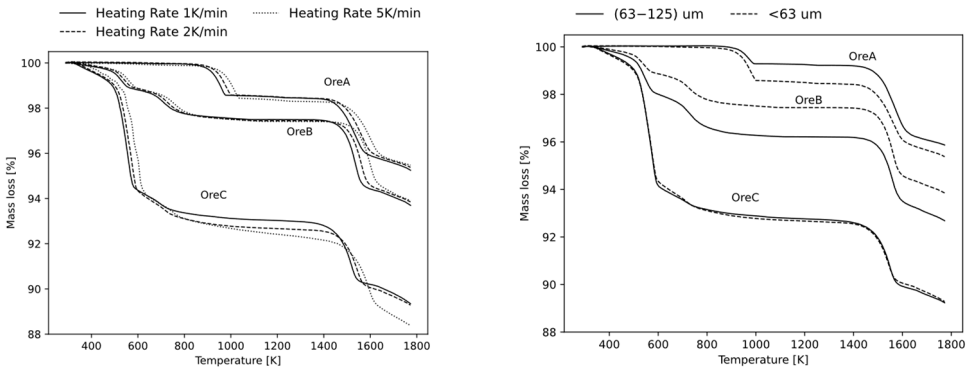

(**a**) (**b**)

Figure 6. Mass loss curves of hematite and goethite ore particles: (**a**) fraction of <63 µm for varying heating rates and (**b**) fraction of <63 µm and (63–125) µm for a heating rate of 2 K/min in non-isothermal conditions.

To obtain details regarding the decomposing gas phases, the off-gas was measured via QMS. Examples of the mass loss curves in combination with the QMS data are presented in Figure 7 for each ore at a heating rate of 2 K/min. Only the main measured gas phases are presented. It must be mentioned that the presented analysis only provides qualitative data, meaning the height of the peaks cannot be compared between experiments. All ores show a distinct O_2 peak at later stages in the reaction. This peak indicates the decomposition of the hematite phase under the removal of oxygen. Above temperatures of 570 °C, the reduction of hematite (Fe_2O_3) occurs step-wise, initially forming porous magnetite (Fe_3O_4) and later wüstite ($Fe_{(1-x)}O$) [14]. Additionally, OreA contains a distinct peak of CO_2 emission. Based on the initial composition of OreA, this peak reflects the decomposition of carbonates (dolomite). The decomposition of dolomite occurs at low CO_2 partial pressures as a single step reaction (Equation (6)) [15].

$$CaMg(CO_3)_2 \rightarrow CaO + MgO + 2CO_2 \quad (6)$$

This behaviour of OreA was also observed in the publication of Chen et al. [10], in which the first mass loss stage was described as calcination (thermal decomposition) of carbonates and the two later mass loss stages were described as the two-stage decomposition of hematite. The QMS signals of OreB and OreC further indicate the emission of water vapour. Water vapour is emitted as the goethite phase converts into hematite based on (Equation (7)) [16].

$$2\alpha FeOOH \rightarrow \alpha Fe_2O_3 + H_2O \quad (7)$$

OreC shows a generally higher mass loss due to the larger amount of goethite in the raw material, leading to a larger (yet, sharp) emission of water vapour. A more continuous emission of water vapour is observed for OreB, indicating a stronger inclusion of the compound in the ore matrix. This behaviour is supported by the Raman spectroscopy presented in Figure 5. It is expected that the goethite present as individual particles is more accessible and therefore decomposes earlier. Consequently, the first stronger peak, which is present for both ores, is assigned to the decomposition of the almost pure goethite particles in the sample. The second peak, as seen in Figure 7b and to lesser extend in Figure 7c, is presumed to be the decomposition of the goethite from the mixed phase or the goethite which is intertwined with hematite in the particles.

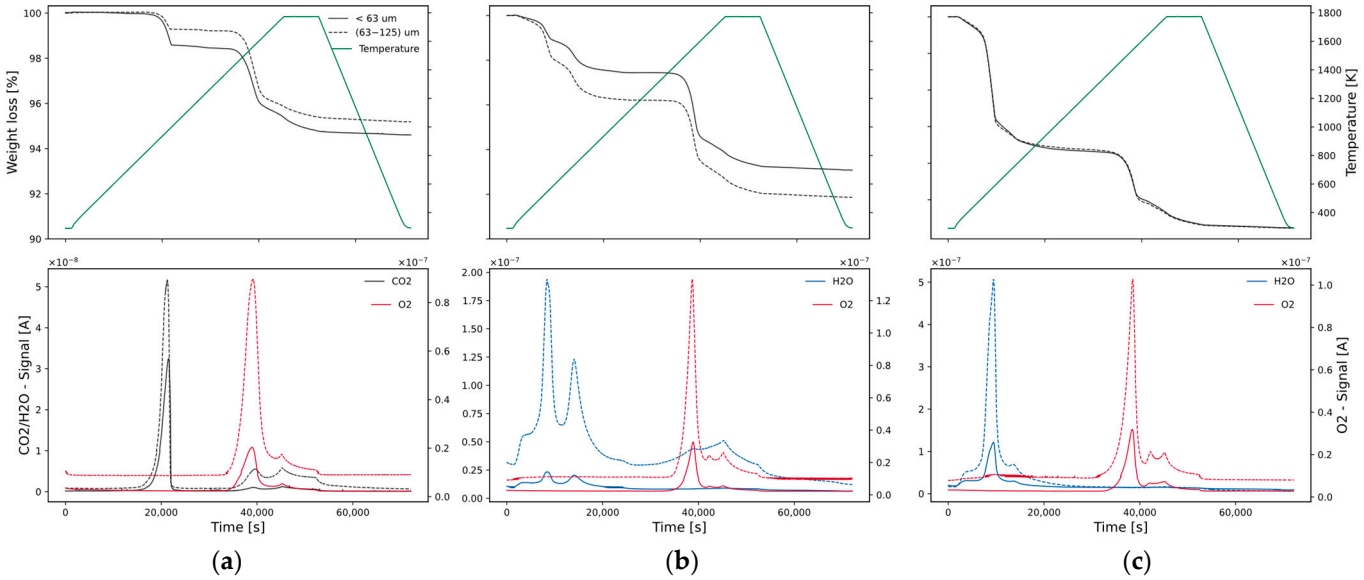

Figure 7. TGA data in combination with temperature profile and QMS data for (**a**) OreA, (**b**) OreB and (**c**) OreC for a heating rate of 2 K/min (solid line: <63 µm size fraction, dotted line: (63–125) µm size fraction).

The start and end temperatures for the individual decomposition stages are determined by the temperature boundaries of the first derivative of the mass loss curves, presented in Table 5 in combination with the measured mass loss in the respective stages. Walter et al. [17] investigated conversion temperatures of goethite to hematite for different particle sizes and observed conversion temperatures between 465 and 523 K. Depending on the particle volume and surface area, they further found either one or two peaks arising in the differential thermal analysis (DTA) measurements. The maximum of the first peak varied between 545 and 551 K and that of the second peak between 578 and 595 K. It is observed in here that, for OreB and OreC, the temperature of the two goethite decomposition stages varies between the two ores. For OreB the decomposition appears in two steps with a similar wide temperature range. Depending on the heating rate, the first stage initiates between 385 and 436 K and ends between 595 and 631 K, exhibiting a mass loss of 0.56% to 0.67%. In comparison, the first decomposition stage of OreC initiates between 395 and 502 K and ends between 616 and 680 K, with a respective mass loss of 3.81% to 4.10%. For OreC, a comparably low mass loss of 0.13 to 0.20% is observed in the second stage. For OreB, the mass loss is similar compared to the first stage (0.55 to 0.65%), with initiation temperatures of 600 to 634 K and ending temperatures of 834 to 917 K. The general higher mass loss of OreC is explained by the higher goethite content in the original ore. Further, the ores vary in average particle size and morphology, possibly influencing the initiation of the peaks.

Chen et al. [10] defined two temperature regions for hematite decomposition. The first stage ranges from 1423 to 1593 K and the second stage is defined as being above 1593 K. Qu et al. [9] observed a similar temperature range for hematite decomposition between 1473 and 1573 K. This study observed slightly lower initiation temperatures for hematite decomposition, between 1312 and 1419 K. Contrary to this study, Chen et al. and Qu et al. used lower amounts of input material and samples differing in particle size and mineralogy from this study, which could be reasons for the variation in the decomposition temperature. Further, Qu et al. only tested a heating rate of 10 K/min and Chen et al., heating rates between 2 and 10 K/min, whereas a higher heating rate usually moves the onset of decomposition to higher temperatures. In the first stage of hematite decomposition, the corresponding mass loss is between 1.95% and 2.66%. The second stage, which begins at temperatures between 1676 and 1743 K, records a significantly lower mass loss, ranging between 0.06% and 0.38%, signifying that most thermal decomposition occurs in the first

stage. Chen et al. [10] compared the significantly larger first stage to the pre-reduction of a particle in suspension, forming clusters with a molten slag phase. The second stage was described to be the reaction of the ores accumulating at the walls of HIsarna, which is in alignment with the differences in weight loss of the two hematite decomposition stages in this study.

Table 5. Decomposition stages of OreA, OreB and OreC for the particle size fraction < 63 µm.

		OreA Heating Rate [K/min]					OreB Heating Rate [K/min]			OreC Heating Rate [K/min]		
		1	2	5			1	2	5	1	2	5
Stage I (Carbonate decomposition)	Start_T [K]	743	719	796	**Stage I (Goethite decomposition)**	Start_T [K]	385	420	436	395	429	502
	End_T [K]	1053	1047	1125		End_T [K]	595	616	631	616	647	680
	Mass loss [%]	1.38	1.38	1.43		Mass loss [%]	0.67	0.56	0.65	4.10	4.06	3.81
Stage II (Hematite decomposition)	Start_T [K]	1325	1397	1382	**Stage II (Goethite decomposition)**	Start_T [K]	600	623	634	621	670	687
	End_T [K]	1687	1625	1724		End_T [K]	834	871	918	793	784	830
	Mass loss [%]	2.28	1.95	2.24		Mass loss [%]	0.55	0.62	0.65	0.20	0.13	0.14
Stage III (Hematite decomposition)	Start_T [K]	1699	1708	1726	**Stage III (Hematite decomposition)**	Start_T [K]	1331	1353	1419	1312	1375	1376
	End_T [K]	-	-	-		End_T [K]	1625	1647	1671	1588	1623	1695
	Mass loss [%]	0.26	0.23	0.06		Mass loss [%]	2.66	2.55	2.23	2.37	2.26	2.09
					Stage IV (Hematite decomposition)	Start_T [K]	1721	1720	1742	1676	1708	1705
						End_T [K]	-	-	-	-	-	-
						Mass loss [%]	0.18	0.13	0.05	0.38	0.14	0.06

4.2. Kinetics of Goethite Decomposition

4.2.1. Influence of Ore Mineralogy

To analyse the conversion of goethite to hematite through the decomposition of OreB and OreC, the conversion results for the particle size fraction of <63 µm, are plotted in Figure 8a. Figure 8b shows the first derivative of the weight loss curves explaining the conversion stages. Two distinctive peaks are visible for both ores, indicating the two decomposition stages of the goethite phase. A conversion factor of 1 equals complete decomposition of the goethite phase to hematite under the release of water vapour, as presented in Equation (7). The initial decomposition of the goethite phase is comparably slow but increases steeply at around 500 K. Due to the strong decomposition of OreC in the first stage, the conversion is steeper throughout the first stage and almost reaches full conversion in this stage. This increase occurs in a short temperature range, and a conversion factor above 0.8 is reached. The conversion in the second stage continues more slowly, until full conversion is reached. Compared to that, OreB conversion occurs over a larger temperature range with a significant amount of conversion occurring in the second stage of goethite thermal decomposition. The differences in conversion can again be explained by the results of the Raman spectroscopy in Figure 5. First, a steep increase in conversion can be expected due to the initial decomposition of almost pure and, therefore, more accessible goethite particles. Since the goethite content in OreC is significantly higher compared to OreB, more conversion happens at lower temperatures, while the conversion of the mixed phases occurs at a later stage.

It is important to understand how the decomposition behaviour influences the decomposition kinetics. The most essential kinetic parameter to determine is the reaction rate constant, containing the activation energy and the pre-exponential factor. The model fitting approach, explained in the previous section, has been applied to the different experimental results regarding goethite decomposition. Based on the best linear fit, the rate-determining models can be evaluated. The R^2 for the linear fit of the different decomposition experiments are presented in Table S1 in the supplementary materials. The bold values of the fitting mark the reaction model, which has been used for further calculations. A number of models were not able to present the experimental data in the second stage of goethite decomposition, due to them violating the assumption that the activation energy needs to be larger than 0. The

assumption-violating models for OreB are the nucleation models P1, P2 and P3 and for OreC they are the nucleation models P1, P2, P3 and P4 and the zero-order reaction model F0. For both ores, the first stage of goethite decomposition appears to be limited by the reaction order, followed by diffusion control for the second stage of goethite decomposition.

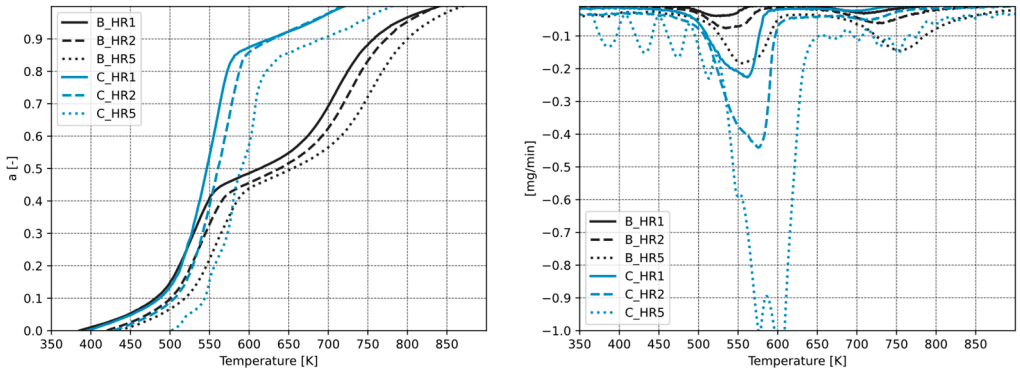

(**a**) (**b**)

Figure 8. Dependency of temperature on (**a**) conversion factor of goethite decomposition for OreB and OreC at varying heating rates (HR) and (**b**) the first derivate of the representative weight loss curves.

Based on the chosen models, the activation energy (Ea) and pre-exponential factor (A) were calculated in order to describe the reaction rate constant (Table 6). The reaction rate constant shows differences depending on the heating rate and ore mineralogy. For OreB the activation energy increases in stage I with the increasing heating rate (46.55 kJ/mol, 56.44 kJ/mol, 60.38 kJ/mol) and decreases with the increasing heating rate in stage II (44.76 kJ/mol, 33.38 kJ/mol, 32.36 kJ/mol). In the case of OreC, no clear trend is observed for the activation energy in stage I. The heating rate of 5 K/min still shows the highest activation energy (134.47 kJ/mol), but the activation energy for the heating rate of 2 K/min (77.86 kJ/mol) is lower compared to the heating rate of 1 K/min (102.62 kJ/mol). The reason for this might be the model selection in the experiment with a heating rate of 1 K/min. For the second decomposition stage, the activation energy again decreases with an increasing heating rate (23.29 kJ/mol, 8.60 kJ/mol, 7.79 kJ/mol). The influence of the heating rate on the activation energy is also observed in further studies [10,18,19]. A difference in the activation energy is visible between the two ores. OreC shows a much higher activation energy in the first decomposition stage and OreB in the second, implying that the two-stage decomposition of OreB is more significant.

Table 6. Reaction rate constant for two stage goethite decomposition of OreB and OreC with respect to heating rate.

Experiments		**Stage I**		**Stage II**	
Ore	**Heating Rate [K/min]**	**Model**	**Rate Constant**	**Model**	**Rate Constant**
OreB	1	F3	$k = 369.27 \frac{1}{min} \times \exp(-\frac{46{,}550 \frac{J}{mol}}{RT})$	D3	$k = 3.06 \frac{1}{min} \times \exp(-\frac{44{,}759 \frac{J}{mol}}{RT})$
OreB	2	F3	$k = 5002.42 \frac{1}{min} \times \exp(-\frac{56{,}441 \frac{J}{mol}}{RT})$	D2	$k = 1.48 \frac{1}{min} \times \exp(-\frac{33{,}378 \frac{J}{mol}}{RT})$
OreB	5	F3	$k = 19.71 \times 10^3 \frac{1}{min} \times \exp(-\frac{60{,}382 \frac{J}{mol}}{RT})$	D2	$k = 2.40 \frac{1}{min} \times \exp(-\frac{32{,}357 \frac{J}{mol}}{RT})$
OreC	1	D3	$k = 9.25 \times 10^6 \frac{1}{min} \times \exp(-\frac{102{,}620 \frac{J}{mol}}{RT})$	D3	$k = 0.17 \frac{1}{min} \times \exp(-\frac{23{,}289 \frac{J}{mol}}{RT})$
OreC	2	F2	$k = 1.24 \times 10^6 \frac{1}{min} \times \exp(-\frac{77{,}860 \frac{J}{mol}}{RT})$	D2	$k = 0.016 \frac{1}{min} \times \exp(-\frac{8459 \frac{J}{mol}}{RT})$
OreC	5	F3	$k = 2.96 \times 10^{11} \frac{1}{min} \times \exp(-\frac{134{,}465 \frac{J}{mol}}{RT})$	D2	$k = 0.025 \frac{1}{min} \times \exp(-\frac{7787 \frac{J}{mol}}{RT})$

Studying the non-isothermal decomposition kinetics of commercial goethite ores, Walter et al. [17] observed activation energies varying between 107.4 and 137.8 kJ/mol for an overall dehydration of goethite, which they compared to the activation energy found

by Pelino et al. [20] (119 kJ/mol) who investigated the decomposition of α-goethite. The activation energies found for the first decomposition stage of OreC are in a similar range, indicating that a difference in ore mineralogy does not have a significant influence on the activation energy. However, considering OreB, with lower goethite contents, the activation energy is lower for both individual stages compared to the overall activation energy values found in the literature. Beuria et al. [21] investigated the isothermal decomposition of iron ores with a goethite content of 47.41 wt.% and found an activation energy ranging between 58.74 and 65.75 kJ/mol, slightly higher compared to stage I of OreB.

4.2.2. Influence of Particle Size

In order to compare the influence of particle size on the decomposition kinetics of industrial goethite ores, TGA experiments of the particle size fractions <63 µm and (63–125) µm were carried out at a heating rate of 2 K/min. Figure 9 compares the conversion factors of OreB and OreC for the two particle size fractions at a heating rate of 2 K/min. The results show that the conversion rate depends more on the goethite content than on the particle size. As concluded from the XRD and XRF measurements in Section 2.1, the amount of crystal water in OreC is similar for both particle sizes (approx. 6 wt.%). In accordance, the course of the conversion over temperature is similar. The results of the particle size comparison of OreB indicate that higher amounts of crystal water can lead to earlier conversion of the goethite phase. The amount of crystal water in the sample of the larger fraction is 3.26 wt.%, compared to 2.19 wt.% in the smaller size fraction. This results in an earlier conversion of the (63–125) µm size fraction. With the increase in particle size, the initiation temperature of the first stage of goethite decomposition of OreB decreases from 420 to 407 K and for the second stage from 623 to 616 K.

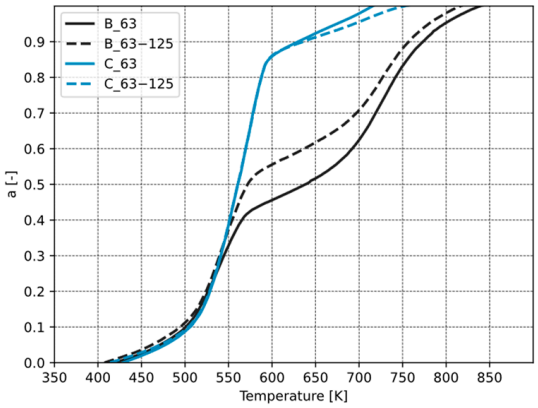

Figure 9. Dependency of particle size on the conversion factor at a heating rate of 2 K/min.

The model fitting approach leads to the same rate-determining mechanism for the different particle size fractions of the same ore (Stage I: chemical reaction; Stage II: diffusion). The kinetic data is displayed in Table 7**.** For OreC, there is a negligible effect of particle size on the conversion factor. As discussed in Section 2.3, the goethite phase is present as a mixed phase with hematite and as a pure phase. The identical reaction mechanisms between the two size fractions indicate that the reaction mechanism is independent of the particle size and more dependent on the nature of the ore. Comparing the reaction rate constants of the larger particle size fractions, a slight influence of the particle size on the activation energy of the goethite decomposition in OreC becomes visible. The activation energy for the larger size fraction (63–125) µm size fraction of OreC is lower for stage I (69.90 kJ/mol) and stage II (3.32 kJ/mol) compared to the activation energy of the smaller size fraction < 63 µm at a heating rate of 2 K/min. For OreB, the activation energy of the (63–125) µm size fraction in stage I (56.26 kJ/mol) is similar compared to the smaller fraction. However, the activation energy calculated for stage II of the larger size fraction of (63–125) µm, 24.43 kJ/mol, is significantly lower compared to the smaller size fraction. The

lower activation energy indicates that the goethite present as a mixed phase with hematite is easily accessible for the larger particle size fraction. The similar activation energy in the first stage of goethite decomposition of OreB indicate a similar behaviour of the initially decomposing pure goethite particles in the samples.

Table 7. Reaction rate constants for two-stage goethite decomposition of OreB and OreC with a size fraction of (63–125) µm.

Stage I				
Ore	Heating Rate [K/min]	R^2	Model	Rate Constant
OreB	2	0.9653	F3	$k = 6659.33 \frac{1}{min} \times \exp(-\frac{56{,}254 \frac{J}{mol}}{RT})$
OreC	2	0.9657	F2	$k = 207273.76 \frac{1}{min} \times \exp(-\frac{69{,}901 \frac{J}{mol}}{RT})$
Stage II				
Ore	Heating rate [K/min]	R^2	Model	Rate constant
OreB	2	0.9461	D2	$k = 0.32 \frac{1}{min} \times \exp(-\frac{24{,}431 \frac{J}{mol}}{RT})$
OreC	2	0.9043	D2	$k = 0.0024 \frac{1}{min} \times \exp(-\frac{3316 \frac{J}{mol}}{RT})$

4.3. Kinetics of Hematite Decomposition

The start temperatures in Table 5 (stage II for OreA and stage III for OreB and OreC) define the beginning of the hematite thermal decomposition. The lowest measured initiation temperature is 1312 K. The non-isothermal decomposition zone is the temperature range of the start temperature in the respective stage until the set temperature of 1773 K is reached. The isothermal zone is the following fixed temperature of 1773 K at a holding time of 2 h. In order to first evaluate the differences in the decomposition behaviour between the ores, the total degree of reduction R[%] at the end of the non-isothermal zone and the total degree of reduction at the end of the isothermal period are presented in Figure 10. The degree of reduction describes how much of the hematite is converted to metallic iron or its intermediate products of magnetite and wüstite, due to the removal of oxygen. The figure shows the degree of reduction depending on time and compares the three ores at individual heating rates. A degree of reduction of 11.11% would indicate a complete conversion from hematite to magnetite. A further increase in the degree of reduction to 33.33% would consequently indicate a full conversion to wüstite. Depending on the heating rate, the degree of reduction of the <63 µm fraction of OreA varies between 9.48 and 10.75% at the end of the non-isothermal zone and between 11.82 and 12.42% at the end of the isothermal zone. These reduction degrees are similar to the reduction degrees achieved by Qu et al. [9] for hematite ores (11.8%). The degrees of reduction at the beginning of the isothermal zone are higher for OreB (11.90–12.90%) and OreC (11.91–13.81%) and increase further until the end of the isotherm (OreB: 14.23–14.57%, OreC: 14.18–16.49%). Comparing the degrees of reduction of the <63 µm size fraction to the (63–125) µm size fraction at a heating rate of 2 K/min, no significant increase in the total degree of reduction is observed for any of the ores (OreA: 12.33% → 12.82%, OreB: 14.23% → 14.34%, OreC: 14.18% → 14.35%). For all ores, the reduction by thermal decomposition is almost completed at the beginning of the isothermal period. The reduction degrees of all the ores indicate that a complete conversion to magnetite occurred and small amounts of wüstite should be present.

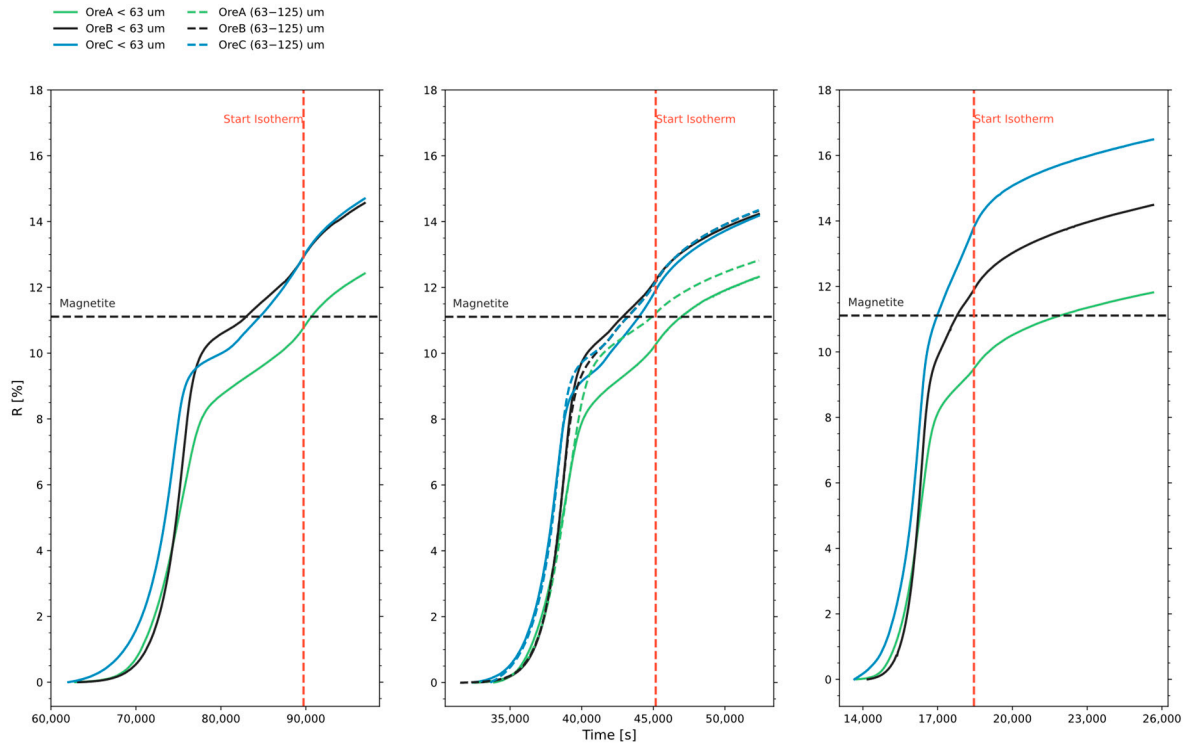

Figure 10. The degree of reduction at the end of the non-isothermal and isothermal heating zone for varying ores and particle sizes at a heating rate of (**a**) 1 K/min, (**b**) 2 K/min and (**c**) 5 K/min (see Table 5 for starting temperatures of hematite decomposition).

In order to validate the presence of the magnetite phase for the further kinetic calculations, example XRD measurements of decomposition products of the size fraction < 63 µm were carried out. For this, a cross-section sample of the solidified material in the crucibles was prepared for analysis. The samples were cut with the Accutom-100 by Struers. Since it was not possible to remove the solidified samples from the crucible, the cross-section was made through the whole crucible. The Alsint crucibles are brittle in nature. Therefore, the cutting spot varies between the samples. The material was solidified by cooling the material in argon atmosphere with a cooling rate of 5 K/min back to room temperature. SEM images of the cross-sections are presented in Figure 11. The sample in the crucible presented in Figure 11a,c was cut vertically, whereas the sample in Figure 11b was cut horizontally.

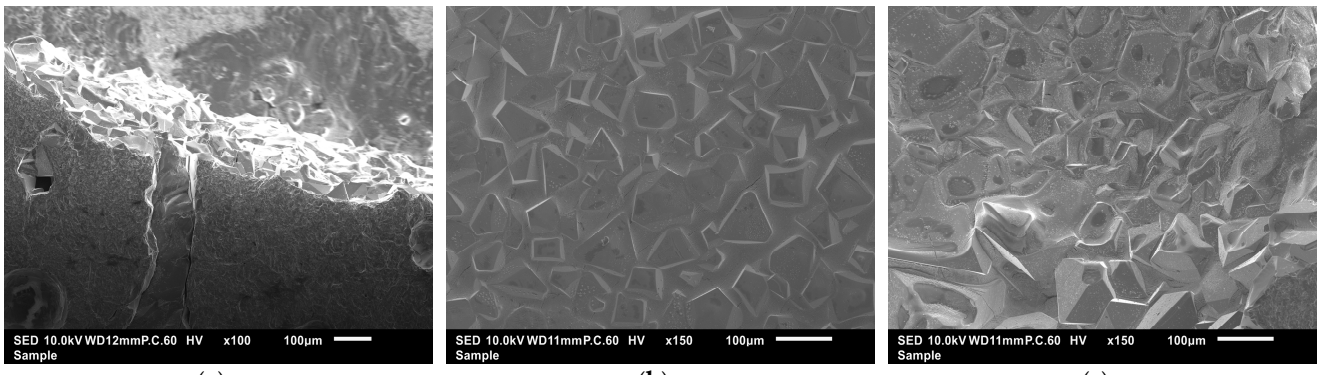

Figure 11. SEM images of cross-sections of (**a**) OreA, <63 µm, heating rate of 2 K/min, (**b**) OreB, <63 µm, heating rate of 2 K/min and (**c**) OreC, <63 µm, heating rate of 5 K/min.

For all observed ores, the cross-section appears similar, showing solidified pre-reduced particles. In contrast to the original ores (Figure 3), the particles now appear in a similar angular shape. The similar shape indicates that the hematite and goethite transitioned to the same iron oxide phase, regardless of the varied initial ore phases. The XRD pattern are displayed in Figure S2 in the supplementary materials. For the samples in Figure 11a,b, the XRD measurements of these cross-sections confirm magnetite as the only iron oxide phase. For the sample in Figure 11c small amounts of fayalite (Fe_2SiO_4) were detected in the XRD pattern next to the magnetite phase. Following the XRD results, magnetite was chosen as the final product for the calculation of the conversion factor of hematite decomposition (Figure 12).

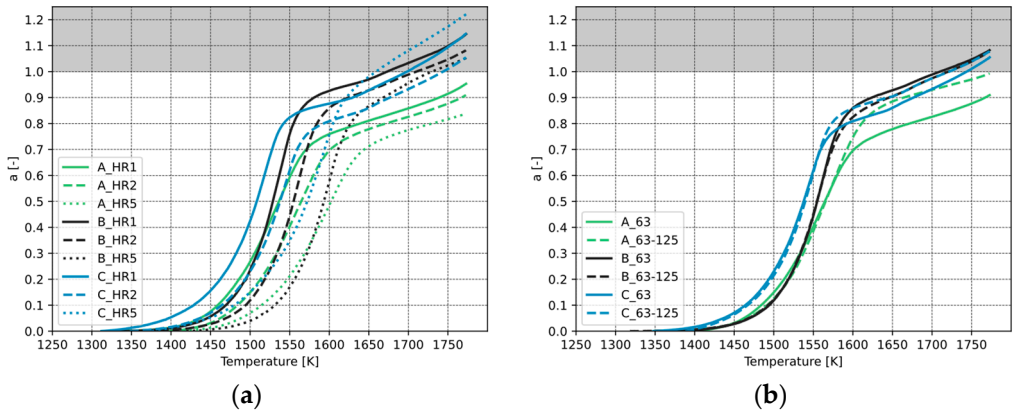

(**a**) (**b**)

Figure 12. Dependency of temperature on conversion factor of hematite decomposition for (**a**) varying heating rates (HR) for a particle size of <63 µm and (**b**) for a heating rate of 2 K/min for particle size of (63–125) µm and <63 µm.

In the following section, only the non-isothermal decomposition kinetic parameters will be calculated. Therefore, for the calculations of the conversion factor the isothermal zone is disregarded. Due to this, the smaller size fraction of OreA does not reach full conversion to magnetite in the presented temperature range. The larger particle size, however, leads to a faster conversion and has reached full conversion to magnetite in the non-isothermal heating zone. Due to the higher reduction degrees in the non-isothermal zone, full conversion to magnetite is reached before the beginning of the isothermal zone for OreB and OreC. The grey area of the figure marks when the conversion factor exceeds unity and the conversion to magnetite is completed and the conversion to wüstite has started already. This area is excluded from the kinetic analysis. OreC shows a faster conversion compared to OreB at all heating rates. In general, a lower heating rate leads to an earlier conversion to magnetite. Model fitting was again applied in order to analyse the present reaction mechanisms of hematite decomposition. As shown in Table 5, most of the decomposition occurs during the first stage (third peak of first derivative) and the influence of the second stage (fourth peak of first derivative) is comparably negligible. Due to this, only the first stage of hematite decomposition is analysed in terms of kinetics. Based on the best linear fit, the rate determining models are evaluated. The R^2 values for the linear fit for the different decomposition experiments for the particle size fraction < 63 µm are presented in Table S2 in the supplementary materials. The bold values in the fitting mark the reaction model, which has been used for further calculations.

Independent of ore mineralogy and heating rate, all model fittings indicate chemical reaction control as reaction mechanism. The hematite decomposition of OreA is a third-order reaction for all heating rates. For OreB and OreC the heating rate influences the order of reaction. For both ores, a heating rate of 1 or 2 K/min leads to a second-order reaction. For OreB, a heating rate of 5 K/min leads to a third-order and for OreC to a first-order reaction. These results contradict the findings of Chen et al. [10], who described the reaction mechanism of hematite decomposition in a temperature range of 1425–1593 K

in non-isothermal conditions as the inner diffusion of iron in the solid phase. The results of our study are more in alignment with the findings of Xing et al. [18], who also found that a second-order reaction as most applicable to the experimental data. The reason for this may be the use of the applied method. As in this study, Xing et al. [18] applied the Coat–Redfern method to determine the kinetic parameters, whereas Chen et al. [10] chose iso-conversional methods to obtain kinetic parameters, before applying them to determine the reaction mechanism. Based on the best-fitting models, the reaction rate constants of the present study were determined and are presented in Table 8.

Table 8. Reaction rate constant of the first stage of hematite decomposition for particle size of <63 µm.

Ore	Heating Rate [K/min]	Model	Rate Constant
A	1	F3	$k = 1.01 \times 10^{17} \frac{1}{min} \times \exp(-\frac{545{,}473 \frac{J}{mol}}{RT})$
A	2	F3	$k = 2.01 \times 10^{21} \frac{1}{min} \times \exp(-\frac{667{,}451 \frac{J}{mol}}{RT})$
A	5	F3	$k = 7.8 \times 10^{17} \frac{1}{min} \times \exp(-\frac{573{,}024 \frac{J}{mol}}{RT})$
B	1	F2	$k = 9.44 \times 10^{20} \frac{1}{min} \times \exp(-\frac{654{,}981 \frac{J}{mol}}{RT})$
B	2	F2	$k = 7.27 \times 10^{20} \frac{1}{min} \times \exp(-\frac{655{,}272 \frac{J}{mol}}{RT})$
B	5	F3	$k = 7.77 \times 10^{26} \frac{1}{min} \times \exp(-\frac{831{,}543 \frac{J}{mol}}{RT})$
C	1	F2	$k = 5.47 \times 10^{15} \frac{1}{min} \times \exp(-\frac{498{,}181 \frac{J}{mol}}{RT})$
C	2	F2	$k = 7.13 \times 10^{15} \frac{1}{min} \times \exp(-\frac{505{,}468 \frac{J}{mol}}{RT})$
C	5	F1	$k = 1.03 \times 10^{13} \frac{1}{min} \times \exp(-\frac{424{,}311 \frac{J}{mol}}{RT})$

Comparing the heating rates of the various ores, no distinct effect of the heating rate is observable. A larger influence is seen for the ore mineralogy. The lowest activation energies are present for OreC, ranging between 424.31 kJ/mol and 505.47 kJ/mol. Higher activation energies were observed for OreA (545.47 kJ/mol–667.45 kJ/mol) and for OreB (654.98 kJ/mol–831.54 kJ/mol). Despite the different methods applied, the activation energy of the first stage of hematite decomposition is in alignment with the activation energy determined by Chen et al. [10] for the first stage of hematite decomposition (636 kJ/mol). The activation energy in the study of Xing et al. [18] was much higher with an average of 1256 kJ/mol. The reason for this may be that the model fit was applied to the overall reaction and not the individual stages of hematite decomposition.

Table 9 presents the reaction rate constants for the larger particle size fractions. The reaction mechanism did not change with the increase in particle size. Directly comparing the results to the smaller size fractions, OreA and OreC show a higher activation energy at an increased particle size. Interestingly, the activation energy of OreB decreases with an increase in particle size to 587.68 kJ/mol at a heating rate of 2 K/min.

Table 9. Reaction rate constant in the first stage of hematite decomposition for particle size of (63–125) µm.

Ore	Heating Rate [K/min]	R^2	Model	Rate Constant
A	2	0.9910	F3	$k = 3.03 \times 10^{21} \frac{1}{min} \times \exp(-\frac{670{,}499 \frac{J}{mol}}{RT})$
B	2	0.9899	F2	$k = 3.18 \times 10^{18} \frac{1}{min} \times \exp(-\frac{587{,}682 \frac{J}{mol}}{RT})$
C	2	0.9773	F2	$k = 6.11 \times 10^{23} \frac{1}{min} \times \exp(-\frac{592{,}322 \frac{J}{mol}}{RT})$

Based on the results, Figure 13 summarises the process of the thermal decomposition of the iron ore used in this study. The illustration shows the decomposition of hematite as only iron-bearing phase (OreA) and the decomposition if both hematite and goethite are present (OreB and OreC) as separated flows. In the decomposition process of OreA, dolomite present in the sample first decomposes, leading to the emission of CO_2. For

OreB and OreC, goethite decomposition occurs as a two-stage process and is the first identified decomposition process. The first stage of goethite decomposition is assumed to be that of the almost pure goethite particles detected with the Raman spectroscopy. The conversion of goethite to hematite in this stage is found to be controlled by the chemical reaction. In the second stage it is expected that the less accessible goethite, which co-exists with hematite in the same particle, decomposes. The decomposition control shifts from a chemical reaction to diffusion in this stage. The decomposition of the goethite phase is identified by the emission of water vapour. For all ores, the last observed decomposition is the conversion from hematite to magnetite under the release of oxygen at elevated temperatures. Independent of the input ore, the hematite conversion initiates at similar temperatures and is found to be controlled by a chemical reaction for all of the ores.

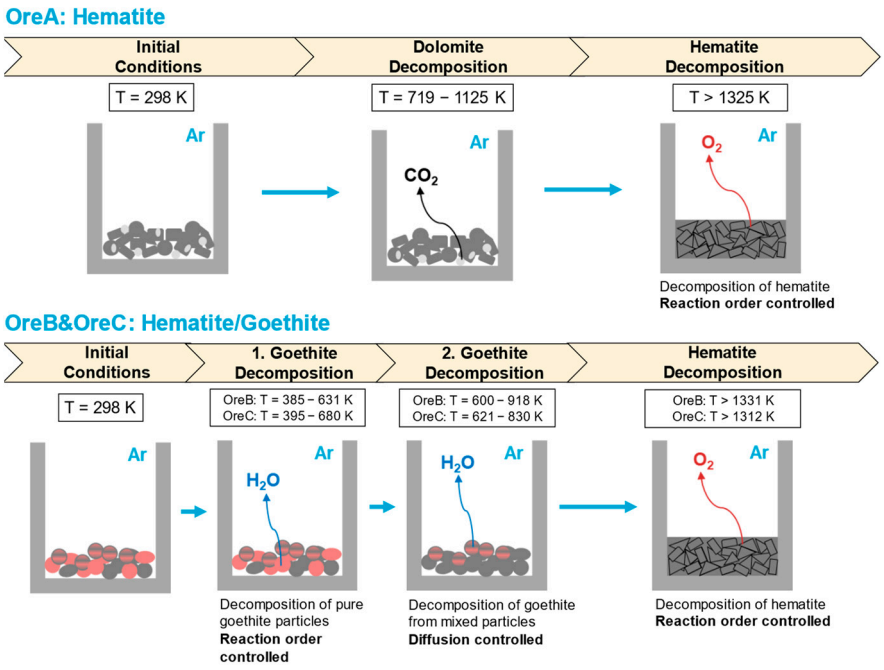

Figure 13. Schematic illustration of the thermal decomposition process of varying iron ore fines.

5. Conclusions

1. The varying raw iron ores investigated in this study (elaborated in Section 2) differ from one another in morphology, mineralogy and chemical composition. However, after the pre-reduction in an argon atmosphere in the TGA experiments at 1773 K, the morphology of the pre-reduced magnetite phases appeared to be identical.
2. The thermal decomposition of goethite ore occurs as a two-stage process. The mass loss in the individual goethite stages depends on the goethite content in the ore. For the particle size fraction of <63 µm, OreB shows two similar mass loss stages, with an observed mass loss of 0.56–0.67 wt.% in the first and 0.55–0.65 wt.% in the second stage. OreC shows stronger differences with a mass loss of 3.81 wt.%–4.10 wt.% in the first and 0.13–0.20 wt.% in the second stage.
3. The proposed reaction mechanisms for goethite decomposition are a chemical reaction in the first stage and diffusion in the second stage (temperature intervals stated in Table 5). The order of reaction and dimension of diffusion partially varied and is difficult to prove due to the nature of the TGA. Therefore, the investigation of reaction order and diffusion dimension will be within the scope of future research. Due to the significant differences in weight loss in both decomposition stages between OreB and OreC, OreC shows higher activation energies in the first stage (77.86–134.47 kJ/mol) and OreB in the second stage (32.36–44.76 kJ/mol) for a particle size fraction < 63 µm.

4. An increase in particle size has no influence on the reaction mechanisms of goethite thermal decomposition. However, the activation energy remains similar for OreB in the first stage (56.44 → 56.26 kJ/mol) but decreases in the second stage (33.38 → 24.43 kJ/mol). The reason for the change in activation energy is proposed to be the difference in mineralogy between the two particle size fractions. The larger fraction of OreB contains higher amounts of crystal water, possibly leading to an easier release in the second decomposition stage. For OreC, however, the activation energy decreases in both stages (77.86 → 69.90 kJ/mol and 8.46 → 3.32 kJ/mol) with increasing particle size, despite a similar level of crystalline water, arguing for the influence of particle size on the activation energy.
5. Hematite thermal decomposition also occurs as a two-stage process, with the first stage initiating between 1311 and 1419 K and the second stage between 1676 and 1742 K, depending on ore composition and heating rate. A significant amount of decomposition takes place in the first stage. The order of highest average total reduction degree for the size fraction < 63 µm is OreC (14.18–16.49%) > OreB (14.23–14.57%) > OreA (11.82–12.42%). At the same heating rate, an increase in particle size leads to no significant increase in the degree of reduction for all ores.
6. The proposed first stage of hematite decomposition is chemical reaction controlled, while the order of the reaction rate depends on the heating rate and ore type. Again, due the nature of the TGA, the order of the reaction is difficult to prove and will be within the scope of future research. No influence of the particle size on the reaction mechanism was observed. The lowest activation energy for the < 63 µm size fraction was found for OreC (424.31–505.47) kJ/mol. A higher activation energy was determined for OreA (545.47–667.45) kJ/mol and OreB (654.98–831.54) kJ/mol. For OreA and OreC the activation energy increases and for OreB it decreases with an increase in particle size.

Supplementary Materials: The following supporting information can be downloaded at: https://www.mdpi.com/article/10.3390/met14111271/s1, Figure S1: XRD pattern of OreA (a), OreB (b) and OreC (c) with the particle size fraction < 63 µm portrait in black and the size fraction (63–125) µm in red; Table S1: Linear regression results of model fitting approach for thermal goethite decomposition (fraction < 63 µm); Table S2: Linear regression results of model fitting approach for hematite thermal decomposition (fraction < 63 µm); Figure S2: XRD patterns of cross-section of OreA, <63 µm, heating rate of 2 K/min, OreB, <63 µm, heating rate of 2 K/min and OreC, <63 µm, heating rate of 5 K/min.

Author Contributions: Conceptualization, P.L.; methodology, P.L.; software, P.L.; validation, P.L. and J.C.B.; formal analysis, P.L. and A.M.A.; investigation, P.L., J.C.B. and A.M.A.; resources, Y.Y. and C.Z.; data curation, P.L.; writing—original draft preparation, P.L.; writing—review and editing, P.L., Y.Y., C.Z., S.T.A., N.D., K.M. and J.v.d.S.; visualisation, P.L.; supervision, Y.Y., C.Z., S.T.A., N.D., K.M. and J.v.d.S.; project administration, Y.Y. and C.Z.; funding acquisition, Y.Y. and C.Z. All authors have read and agreed to the published version of the manuscript.

Funding: This research was carried out under project number T20009 in the framework of the Research Program of the Materials innovation institute (M2i) (www.m2i.nl) supported by the Dutch government.

Data Availability Statement: The original contributions presented in the study are included in the article, further inquiries can be directed to the corresponding author.

Acknowledgments: Ruud Hendrikx and Richard Huizenga at the Department of Materials Science and Engineering of the Delft University of Technology are acknowledged for the XRD analysis.

Conflicts of Interest: The authors declare no conflicts of interest.

References

1. Worldsteel Association. *Climate Change and the Production of Iron and Steel*; Worldsteel Association: Brussels, Belgium, 2021.
2. Worldsteel Association. *Sustainable Performance of Steel Industry 2003–2021*; Worldsteel Association: Brussels, Belgium, 2022.
3. Worldsteel Association. *2022 World Steel in Figures*; Worldsteel Association: Brussels, Belgium, 2022.

4. Yang, Y.; Raipala, K.; Holappa, L. Ironmaking. In *Treatise on Process Metallurgy*; Elsevier Ltd.: Amsterdam, The Netherlands, 2014; Volume 3, pp. 2–88. [CrossRef]
5. Biwas, A.K. *Principles of Blast Furnace Ironmaking: Theory and Practice*; Cootha Publishing House: Brisbane, Australia, 1981.
6. Naito, M.; Takeda, K.; Matsui, Y. Ironmaking Technology for the Last 100 Years: Deployment to Advanced Technologies from Introduction of Technological Know-how, and Evolution to Next-generation Process. *ISIJ Int.* **2015**, *55*, 7–35. [CrossRef]
7. Meijer, K.; Guenther, C.; Dry, R.J. *HIsarna Pilot Plant Project*; METEC InSteelCon 2011: Düsseldorf, Germany, 2011.
8. Meijer, K.; Zeilstra, C.; Teerhuis, C.; Ouwehand, M.; van der Stel, J. Developments in Alternative Ironmaking. *Trans. Indian Inst. Met.* **2013**, *66*, 475–481. [CrossRef]
9. Qu, Y.; Yang, Y.; Zou, Z.; Zeilstra, C.; Meijer, K.; Boom, R. Thermal decomposition behaviour of fine iron ore particles. *ISIJ Int.* **2014**, *54*, 2196–2205. [CrossRef]
10. Chen, Z.; Zeilstra, C.; Van Der Stel, J.; Sietsma, J.; Yang, Y. Thermal Decomposition Reaction Kinetics of Hematite Ore. *ISIJ Int.* **2020**, *60*, 65–72. [CrossRef]
11. Hanesch, M. Raman spectroscopy of iron oxides and (oxy)hydroxides at low laser power and possible applications in environmental magnetic studies. *Geophys. J. Int.* **2009**, *177*, 941–948. [CrossRef]
12. Coats, A.W.; Redfern, J.P. Kinetic Parameters from Thermogravimetric Data. *Nature* **1964**, *201*, 68–69. [CrossRef]
13. Pourghahramani, P.; Forssberg, E. Reduction kinetics of mechanically activated hematite concentrate with hydrogen gas using nonisothermal methods. *Thermochim. Acta* **2007**, *454*, 69–77. [CrossRef]
14. Sun, S.S. A Study of Kinetics and Mechanisms of Iron Ore Reduction in Ore/Coal Composites. Ph.D. Thesis, McMaster University, Hamilton, ON, Canada, 1997.
15. Otsuka, R. Recent studies on the decomposition of the dolomite group by thermal analysis. *Thermochim. Acta* **1986**, *100*, 69–80. [CrossRef]
16. Diamandescu, L.; Mihàilà-Tàràbàşanu, D.; Feder, M. On the solid phase transformation goethite → hematite. *Mater. Lett.* **1993**, *17*, 309–311. [CrossRef]
17. Walter, D.; Buxbaum, G.; Laqua, W. The Mechanism of the Thermal Transformation From Goethite to Hematite. *J. Therm. Anal. Calorim.* **2001**, *63*, 733–748. [CrossRef]
18. Xing, L.; Qu, Y.; Wang, C.; Shao, L.; Zou, Z.; Song, W. Kinetic Study on Thermal Decomposition Behavior of Hematite Ore Fines at High Temperature. *Metall. Mater. Trans. B* **2020**, *51*, 395–406. [CrossRef]
19. Sun, Y.; Han, Y.; Wei, X.; Gao, P. Non-isothermal reduction kinetics of oolitic iron ore in ore/coal mixture. *J. Therm. Anal. Calorim.* **2016**, *123*, 703–715. [CrossRef]
20. Pelino, M.; Toro, L.; Petroni, M.; Florindi, A.; Cantalini, C. Study of the kinetics of decomposition of goethitein vacuo and pore structure of product particles. *J. Mater. Sci.* **1989**, *24*, 409–412. [CrossRef]
21. Beuria, P.C.; Biswal, S.K.; Mishra, B.K.; Roy, G.G. Study on kinetics of thermal decomposition of low LOI goethetic hematite iron ore. *Int. J. Min. Sci. Technol.* **2017**, *27*, 1031–1036. [CrossRef]